ORNL/TM-2022/2486

Eddy Current Flow Meter Measurements and Modeling Validation

Cornwall Lau
Sacit Cetiner (INL)
Venu Varma
Eliott Fountain
Paul Groth
Craig Mauer
Dustin Ottinger
Bruce Warmack

June 2022

OAK RIDGE National Laboratory

ORNL IS MANAGED BY UT-BATTELLE LLC FOR THE US DEPARTMENT OF ENERGY

ORNL/TM-2022/2486

Fusion Energy Division

EDDY CURRENT FLOW METER MEASUREMENTS AND MODELING VALIDATION

Cornwall Lau
Sacit Cetiner (Idaho National Laboratory)
Venu Varma
Eliott Fountain
Paul Groth
Craig Mauer
Dustin Ottinger
Bruce Warmack

June 2022

Prepared by
OAK RIDGE NATIONAL LABORATORY
Oak Ridge, TN 37831-6283
managed by
UT-BATTELLE LLC
for the
US DEPARTMENT OF ENERGY
under contract DE-AC05-00OR22725

CONTENTS

ABSTRACT

The goal of the eddy current flow meter (ECFM) is to monitor velocities and temperatures of conductive liquid metals. The ECFM can also detect voids in two-phase liquid metal flows. Measurement of these flows can greatly improve the accuracy of the empirical formulas used for fluid dynamics near the reactor core and aid in mapping any non-uniformities in fluid flow such as estimates of temperature and phase. While the eventual goal is to develop the ECFM for the liquid sodium surrounding the Versatile Test Reactor (VTR) core, this report focuses on modeling and experimental validation of ECFM for a moving solid test rod and for liquid mercury in the Target Test Facility (TTF) flow loop to better understand and further develop ECFM measurement capabilities by validating model predictions with benchmark experiments. Eventually the models could be used to design and optimize future ECFMs for specific applications such as monitoring flow within the VTR pool.

1. INTRODUCTION

1.1 Objectives of This Report

Development and testing of the ECFM is necessary to characterize optimal sensor parameters and performance for a given environment. This includes but is not limited to sensor size, sensitivity, maintainability, reliability and duration of use. The overall objectives of this work are as follows:

- Development of computational models that characterize ECFM performance
- Validation of computational models for a wide range of benchmark experiments
- Design and optimization of ECFM sensors for experiments such as VTR

The importance of a validated ECFM model is multifaceted. First, creating an experimentally validated sensor model reduces the effort necessary for future installations of the ECFM to be designed and calibrated. This saves on cost and reduces installation and setup calibration times such as measuring the velocity surrounding the reactor core [1]. Additionally, it can be used in more detailed system simulations of the reactor's operation, improving future studies in sensors and controls, data science, and computational fluid dynamics[2].

The development of a computational model to characterize ECFM performance was a focus of a previous report[3] so only a brief summary is given here. Some changes were made to the computational model and those changes are highlighted in this report. The major goal of this report is validation of computational models on a moving, electrically conducting solid rod and liquid mercury experiments. These benchmark experiments were chosen for numerous reasons. Starting with a low-temperature, non-toxic solid rod avoids the safety-issues associated with high-temperatures and toxic liquid metals. Additionally, the solid rod is more accessible, provides better knowledge and control of the velocity profile, and allows quicker modifications to the experiment to understand sensor performance. Once understanding of the solid rod experiment is completed, experiments on a liquid mercury test loop allows for testing in at low-temperatures liquid flows before moving to high-temperatures liquid metal benchmark experiments in future years. This report shows both modeling and measurement results for a moving solid rod and liquid mercury.

1.2 Organization of This Report

Section 2 of this report discusses the background for this ECFM sensor project. Section 2.1 briefly discusses the ECFM theoretical and experimental concept and section 2.2 discusses the Target Test

Facility (TTF). Section 3 discusses the experimental and modeling setup for both the solid rod and TTF loop. Section 3.1 focuses on the ECFM experimental setup and procedure and section 3.2 focuses on the ECFM modeling setup and procedure. Section 3.3 focuses on computational fluid dynamics modeling. Section 4 presents the experimental and modeling results. Section 4.1 presents the experimental and modeling results for the solid rod and section 4.2 presents the experimental and modeling results for TTF. Section 5 concludes this report.

2. BACKGROUND

2.1 ECFM Theoretical and Experimental Concept

The ECFM concept has been described in many previous reports and papers[3], [4]. Only a brief description is given here. One of the goals of this project is to install a ECFM to measure flows on the liquid mercury TTF loop [5] at Oak Ridge National Laboratory (ORNL). This has also been discussed in detail in previous reports and papers and only a brief description of TTF is also given here.

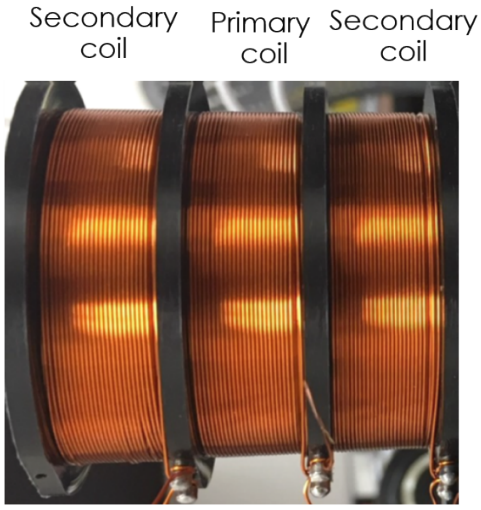

Figure 1. Example ECFM sensor.

The ECFM discussed here consists of one primary coil and two secondary coils. An example is shown in Fig. 1. An alternating current (AC) is excited in the primary coil for a given AC current and frequency. If there is a velocity, $\vec{v}$, in an electrically conductive medium, an AC eddy current can be produced at the given excited frequency. This is often expressed mathematically in the induction equation, which is shown in Eq. (1).

$$\frac{\partial \vec{B}}{\partial t} = \nabla \times \left(\vec{v} \times \vec{B}\right) + \frac{1}{\mu\sigma}\nabla^2\vec{B} \qquad (1)$$

$\vec{B}$ is the AC magnetic field, σ is the electrical conductivity, and μ is the magnetic permeability. Using the vector magnetic potential, a time-harmonic representation of the vector fields with angular frequency, ω, and adding in an external excitation source, $\vec{J}_{ext}$, results in Eq. (2). This Eq. (2) is the equation that is simulated in this report and discussed in Section 3.

$$\nabla^2\vec{A} - \mu\sigma\left(\vec{v} \times \left(\nabla \times \vec{A}\right)\right) + j\omega\sigma\vec{A} = \mu_0\vec{J}_{ext} \qquad (2)$$

This eddy current can be measured in an ECFM by measuring the voltage difference in the secondary coils divided by the amplitude of the alternating current. This is often referred as the sensitivity. There are many experimental examples of ECFMs in the literature, so only a brief description is given here. A recent summary of the history of eddy current flow meters to measure flows in electrically conductive liquid metals is discussed in [4]. A more relevant report has also been recently collated on the ECFM that was installed in the liquid sodium cooled Fast Flux Test Facility (FFTF) nuclear test reactor [5]. The geometry of the bobbin and the number of coils are important parameters that determine the sensitivity of the ECFM sensor. This particular sensor is intended for room-temperature non-toxic applications, so the coils can be made out of polymer insulated copper and the bobbin can be made out of acetal plastic. For applications in nuclear test reactors, different materials need to be chosen and example materials are described in reference [5] for the FFTF nuclear test reactor. The goal of this report is demonstrate that electromagnetic finite element modeling can be used to design such a ECFM sensor, as shown by benchmarking to dry solid conducting rod experiments and liquid mercury experiments.

2.2 Target Test Facility

The Target Test Facility (TTF) is a full-scale replica of the Spallation Neutron Source (SNS) Target Cell mercury flow loop. The flow loop includes a 75-horsepower centrifugal pump, a mock heat exchanger, storage tank, simulated target module, numerous pipes up to 10 inches in diameter, pipe couplings, valves, and various diagnostics and sensors. The TTF process is instrumented to provide information regarding the flow rate, pressure, and temperature of the mercury in the process loop.

The TTF contains approximately 1.4 cubic meters of elemental mercury (Hg) weighing approximately 42,000 lbs. The TTF has multiple purposes. Firstly, it is used to study the thermal and hydraulic flow characteristic of the mercury in the target to provide sufficient information to be able to subsequently design the target module. Secondly, it is used to develop the remote handling techniques and tools for maintaining the SNS target cell equipment including the target module.

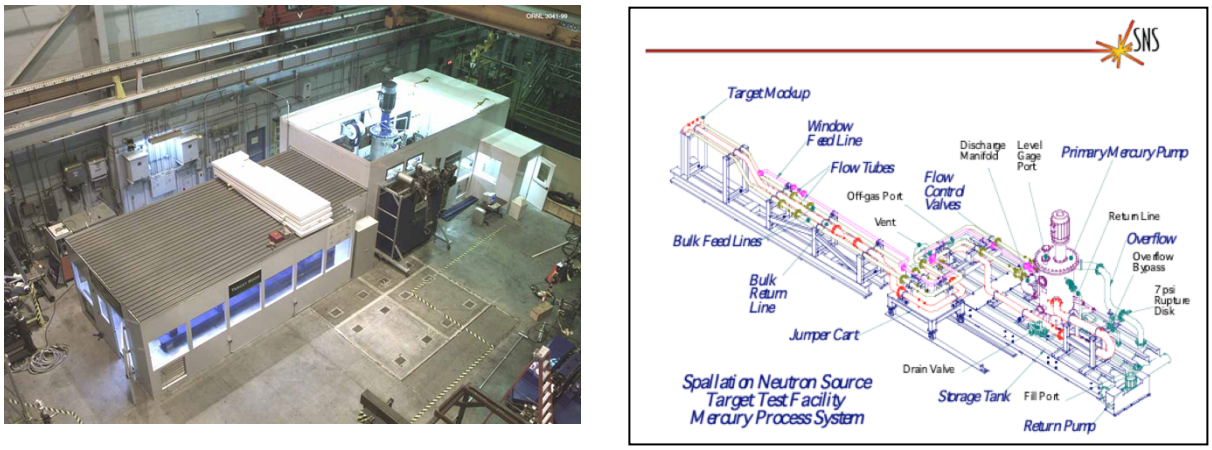

Figure 2. Aerial View of the TTF facility and a schematic of the mercury loop

The TTF is located in the high bay facility (Building 7603) of the Fusion Energy Division at Oak Ridge National Laboratory. This is shown in Fig. 2. The TTF covers approximately 2000 sq. ft. of floor space. The presence of mercury in the system requires that the test loop be maintained in an enclosure that provides secondary containment for mercury. The enclosure also includes a ventilation system designed for five air exchanges an hour, special ventilation duct carbon filters, mercury monitors, and clean up/spill equipment.

3. EXPERIMENTAL AND MODELING SETUP

3.1 ECFM Experimental Setup and Procedure

As discussed in the objectives of this report, one of the major goals is to validate computational models with benchmark experiments. This validation should be done over a wide range of parameters. This can include the excited AC frequency and amplitude, material properties such as electrical conductivity and magnetic permeability of the solid or liquid medium, flow velocity and size of the solid or liquid medium, and geometry and number of coil windings in the bobbin. While not all these parameters can be varied easily, effort has been made to vary as many of these parameters as possible in the experimental setup to assess their impact on measurement performance and to help validate the computational models. This section details the experimental setup and procedure for both a solid rod and liquid mercury experiment.

3.1.1 ECFM Experimental Setup and Procedure for Solid Rod

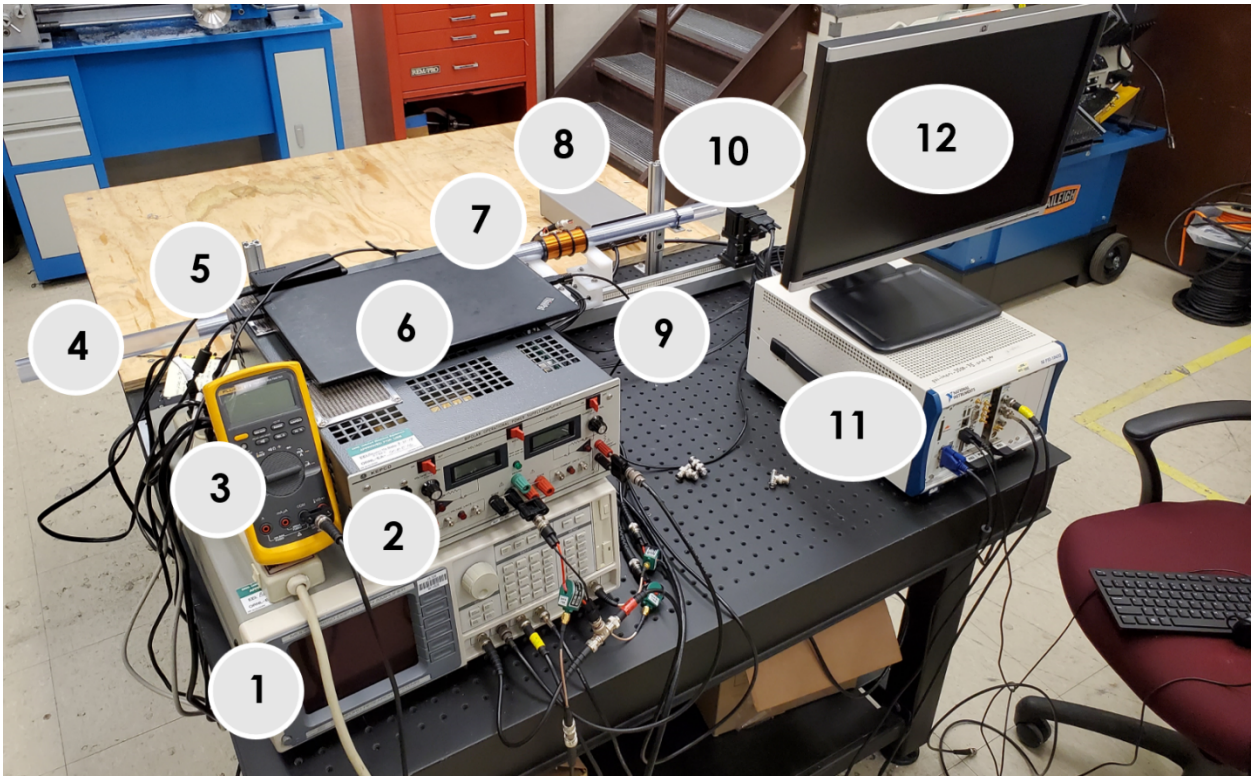

Figure 3. 1. Dual-phase Lock-in amplifier. 2. 20 V power supply 3.Multimeter. 4. PVC plastic pipe. 5. Conducting rod. 6. Laptop. 7. Bobbin. 8. Servo motor controller. 9. Linear Actuator. 10. Servo motor. 11. PXI digitizer and controller. 12. Monitor.

An image of the experimental setup for measuring the ECFM sensor response of a solid conducting rod is shown in Fig. 3. 12 components of the experimental setup are labelled in Fig. 2 and consists of a dual-phase lock-in amplifier, 20 V power supply, multimeter, PVC plastic pipe, conducting rod, laptop, bobbin., servo motor controller, linear actuator, servo motor, PXI digitizer and controller, and monitor. Various parameters can be changed in this experimental setup and is shown in Table 1. The parameter range scanned in this report is also shown in Table 1.

Parameter	Parameter Range
Solid Rod material	6061-T6 aluminum or 316L stainless steel
Pipe material	PVC plastic
Bobbin velocity	Up to 0.5 m/s in either direction of the linear actuator
Bobbin geometry	3 bobbins varying in number of coils and coil width
Excited AC amplitude	Up to 1 A
Excited AC frequency	25 to 1000 Hz

Table 1. List of parameters varied in this experimental setup for the solid dry rod.

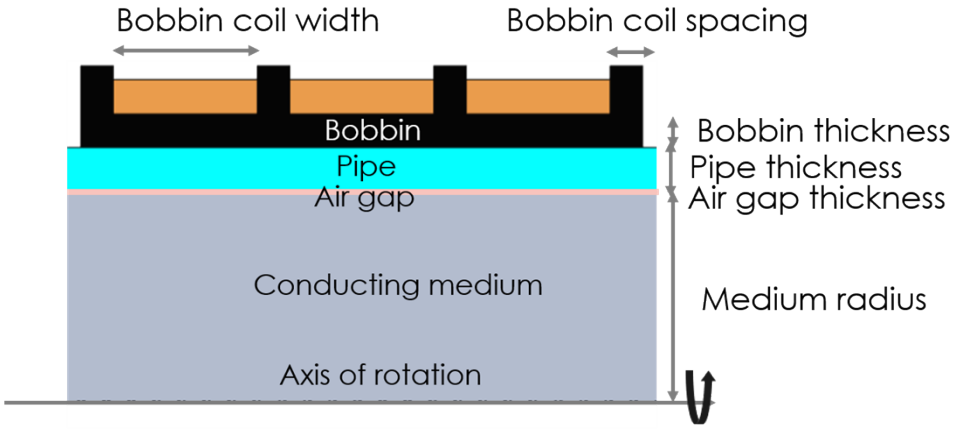

Figure 4. Geometry of the bobbin, pipe, and conducting medium.

Parameter	Bobbin #1	Bobbin #2	Bobbin #3
Bobbin axial coil spacing	2.54 mm	2.54 mm	2.54 mm
Bobbin radial thickness	2.54 mm	2.54 mm	2.54 mm
Bobbin axial coil width	11.75 mm	23.96 mm	24.86 mm
Bobbin coil gauge diameter	0.452 mm	0.452 mm	0.452 mm
Number of coil turns in each coil	6	3	6
Number of coils in (S,P,S) coils	156,160,156	158,159,155	325,326,325

Table 2. Geometry of the bobbin for the dry rod experiments.

The geometry of the bobbin, conducting medium, and pipe is shown in Fig. 4. For this dry rod test, the conducting medium is a solid 6061-T6 aluminum rod or solid 316L stainless-steel (SS) rod. The pipe is PVC plastic. The aluminum rod has a 25.4 mm diameter. The SS rod has a measured diameter of 25.6 mm. The schedule 40 PVC pipe has a thickness of 3.3782 mm and inner diameter of 26.6446 mm. An air gap therefore exists between the PVC pipe and solid rod so that the rod can fit inside the pipe. The air gap is calculated to be 0.52 and 0.62 mm, respectively, for the SS and aluminum rod. A choice of one of three different bobbins can be attached to the experimental setup. The bobbins intentionally differ in the coil length and number of coils with the full details shown in Table 2. The bobbins are manufactured from acetal plastic and then the copper coils are winded using a coil winding station. Due to some manufacturing issues, the number of coils and coil lengths are different from the specifications and the measured ones are shown in Table 2.

To operate this experimental setup to measure the ECFM sensor sensitivity, the lock-in amplifier drives a sine waveform that controls the excited AC frequency and amplitude. This waveform is amplified by a 20 V KEPCO bipolar power supply that can be used in constant current operation and can supply AC currents with 3-dB frequency bandwidth up to 10000 Hz. The output of the power supply is then fed into both the primary coil of the ECFM bobbin and a multimeter. The multimeter is used to measure the amplitude of the AC current. The bobbin can be moved forward or backward on a linear motion actuator

using a motor and servo motor controller. A laptop is used to control the servo motor controller and consequently the motion of the bobbin. The velocity of the bobbin on the linear actuator drive can be recorded on the laptop.

When an AC current is applied on the primary coil, induced currents and voltages are driven on the two secondary coils of the bobbin. If the bobbin is not moving, this induced voltage in each of the secondary coils is nominally equal and the difference of the induced voltage is nominally zero. If the bobbin is moving, the difference of the induced voltage is nominally non-zero. This induced voltage on each of the secondary coils is wired into a Pearson 2878 probe (explained below) that is wired differentially to the lock-in amplifier and converts the voltage to a current measurement. This method removes any possible impedance mismatches caused by the inductive coil and measurement device, as the current probe has only a 50 Ω output resistance. The dual-phase lock-in amplifier automatically calculates the difference of the AC currents in the two secondary coils, amplifies this AC current difference using a built-in amplifier, and converts this complex AC difference into a direct current (DC) signal whose in-phase and quadrature signals are then outputted and recorded with a PXI digitizer using a custom-made LabView script. The amplification should be set as high as possible for signal to noise within the voltage range of the PXI digitizer. For the dry solid rod cases shown in this paper, a 40 dB gain is used.

Accurate accounting of the frequency response to the Pearson 2878 current probe is necessary for this measurement. The Pearson probe nominally has an output of 0.1 Volt per Ampere in their datasheet and an approximate low frequency 3dB point at 30 Hz. Measurements of this Pearson 2878 probe output as a function of frequency has been obtained in a well-known constant current power supply using the AC voltage measurement of a multimeter. This is shown in Fig. 5. The measured output of the Pearson probe is close to expected with an estimated 0.1 V per Ampere for most of the frequency range. At low frequencies, the output does decrease significantly, with an estimated low frequency 3dB point between 10 and 20 Hz. This measured output is used to appropriately calibrate the digitizer DC voltages to the AC current difference between the two secondary coils.

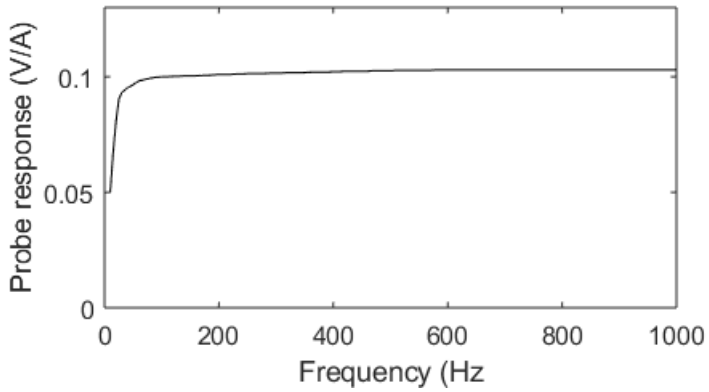

Figure 5. Measured output of the Pearson 2878 probe as a function of frequency.

$$Sensitivity = \tilde{V}/I = \tilde{I}_{exp} * \tilde{Z}/I = \frac{(\tilde{I}_{for} - \tilde{I}_{back})}{2} * \tilde{Z}/I \quad (3)$$

The AC current is the measured signal, but the COMSOL model has sensitivity as its main output. To convert the current to sensitivity to compare between modeling and experiment, knowledge of the impedance is necessary. Mathematically, this is shown in Eq. (3) where $\tilde{V}$, $\tilde{I}$, and $\tilde{Z}$ are the AC voltage, current, and impedance of the upstream (u) and downstream (d) secondary coils respectively. I is the excited AC current amplitude in the primary coil. The sensitivity, $\tilde{V}$, is calculated from the COMSOL simulations [6] , but $\tilde{Z}$ needs to be measured experimentally. For each secondary coil of a bobbin, a signal

impedance analyzer is used to measure this impedance to obtain the desired sensitivity. This impedance measurement varies with excited frequencies, bobbins, rod geometry and material, and pipe geometry and materials, so it needs to be measured in many cases. Fig. 6 shows the impedance measurement of bobbin #1 for one of the secondary coils over a large range of frequency for an aluminum rod and PVC pipe. The impedance is the sum of the resistance and reactance terms where $\tilde{Z} = \tilde{R} + j\omega\tilde{L}$. The AC resistance is relatively constant over frequency with a slight increase at higher frequencies because of skin and proximity effect. The reactance term is dominated by the inductive term, which approximately increases linear with frequency. Therefore, at low frequencies, the impedance is largely determined by the resistive term. For bobbin #1, this occurs for frequencies less than ~100 Hz. At high frequencies, the impedance is largely determined by the reactance term. For bobbin #1, this occurs for frequencies greater than a few hundred Hz. Because the number of coils can be different depending on the upstream and downstream coil, there are observed differences on the order of 1% between the upstream and downstream secondary coils. In this report, it is assumed that $\tilde{Z}$ is the average of the AC impedance of the upstream and downstream coil secondary coils.

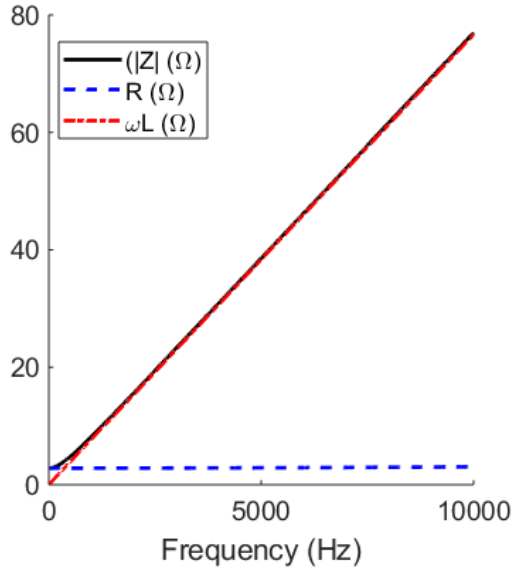

Figure 6. The magnitude of the impedance, resistance, and inductance for bobbin #1 is shown.

Many measurements have been taken for this report and will be reported in a later section. The experimental dataset is reproducible under the same conditions to within a few percent. While there is little variation within a few seconds of a similar experiment, some variation does seem to occur over time periods of hours and days, likely due to temperature variations in the experimental setup, as there is no temperature control in the current experimental setup. Another surprising feature of this experimental dataset, however, is that the in-phase and quadrature signal is measured to be non-zero and varying along the actuator even when the velocity of the bobbin is zero. This is likely due to variations in air gap and diameter along the actuator that can cause the signal to vary substantially. This difference in the in-phase and quadrature signals at zero velocity along the actuator can often be larger than the desired sensitivity signal when the bobbin is moving. To remove this undesired effect, a zero-velocity calibration is done by subtracting the measured in-phase and quadrature signal during forward and backward motion of the bobbin and dividing by 2. Mathematically, this is equivalent to $\tilde{I}_{exp} = \frac{(\tilde{I}_{for} - \tilde{I}_{back})}{2}$ in Eq. (3). By doing this, the zero-velocity contribution to the in-phase and quadrature signals are cancelled out and do not contribute to the result. The square root of the sum of the square of the calibrated in-phase and quadrature signal is the measured experiment AC current, $\tilde{I}_{exp}$. The mean of $\tilde{I}_{exp}$ over the duration of the bobbin

motion is then used in all the subsequent experimental figures. The standard deviation of $\tilde{I}_{exp}$ is used as the error bars. These error bars are therefore statistical and do not represent any systematic errors.

An example for this data analysis approach is shown in Fig. 7 for an example case. In Fig. 7 left), the in-phase signal during the forward motion of the bobbin is shown by the blue dashed line and in-phase signal during the backward motion of the bobbin is shown by the red-dashed line before the zero-velocity calibration for a 0.5 A, 200 Hz excited current and frequency, 0.3 m/s case with an aluminum rod and PVC pipe. In Fig. 7 right), the quadrature signal during the forward motion of the bobbin is shown by the blue dashed line and in-phase signal during the backward motion of the bobbin is shown by the red-dashed line before the zero-velocity calibration for a 0.5 A, 200 Hz excited current and frequency, 0.3 m/s case with an aluminum rod and PVC pipe. Note that the signals for the backward motion have been reversed in time so that the x-axis is at the same axial location along the actuator at each time. The result of the zero-velocity calibration by subtracting the forward and backward motion signals is shown in the solid black line. The bobbin is stationary at the beginning and end of the pulse when the black solid line is zero and the bobbin is moving in the middle of this duration when the black pulse is non-zero. During the motion of the bobbin, there are substantial variations in the raw in-phase and quadrature signals. At each location along the actuator, the signals for backward and forward motion are strongly correlated, indicating that there are variations in the ECFM signal even at zero velocities along the linear actuator. This signal variation has been also confirmed with ECFM signal measurements at zero velocities along the linear actuator. As shown in Fig. 7, the resulting (forward – backward)/2 signal is significantly cleaner and varies considerably less as the bobbin moves along the linear actuator. This data analysis approach for the zero-velocity calibration has proven remarkably robust over the entire range of parameters scanned in this experimental dataset. Besides this zero-velocity calibration, no additional software filtering is done in the data analysis.

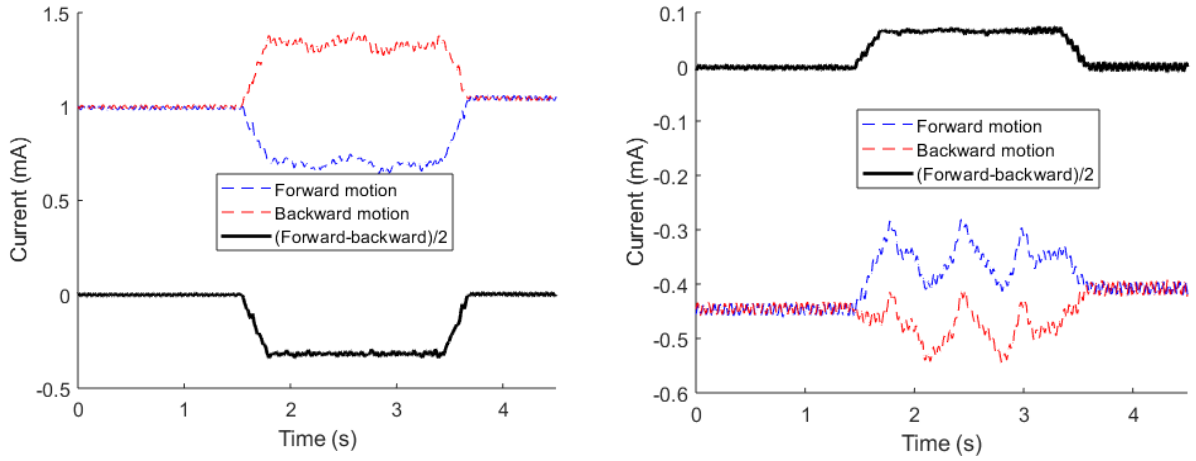

Figure 7. Left) Raw in-phase signal for forward, backward and (forward-backward)/2 motion for a 200 Hz, 0.3 m/s, 0.5 A case with bobbin #3 with an aluminum rod and PVC pipe. Right) Raw quadrature signal for forward, backward and (forward-backward)/2 motion for a 200 Hz, 0.3 m/s, 0.5 A case for bobbin #3 with an aluminum rod and PVC pipe.

3.1.2 Experimental Setup for Liquid Mercury

Fig. 8 shows a drawing of the flow experiment on TTF. The mercury is circulated through the loop by a 75 hp centrifugal pump. Flow rate is controlled by adjusting the speed of the circulation pump in a range from 150 to 400 RPM. The mercury is normally held in a storage tank until operation of the loop is

desired. A vacuum pump is used to evacuate air from the loop. Once sufficient vacuum is achieved, the mercury is transferred from the storage tank to the loop and sump tank. After the transfer process is complete, helium is then backfilled to the sump tank to reach atmospheric pressure.

Upon startup, mercury exits the sump tank and is split into 3 separate lines, two large bulk flow and one reduced auxiliary flow. These three lines will eventually converge into one return flow line back to the sump tank. The ECFM test stand is connected to the auxiliary flow line. The ECFM test stand mercury flow rate is controlled in two ways. The first is by adjusting the speed of the TTF circulation pump. The second is by adjusting a quarter turn ball valve controlling the auxiliary flow line. The flow rate is monitored using multiple V-cone (inverted Venturi tube) flow meters throughout the TTF loop and one within right before the ECFM test stand.

The ECFM flow test stand uses three different tube diameters ranging from 31.75 to 25.4 to 19.05 mm. By using an interconnected tube configuration comprising of at least 600 inch straight sections for each diameter, the distance between each bend will be 10 times larger than the diameter of each pipe with the intended goal of allowing for fully developed flow in each section where the sensors will be placed. Since mass balance has to be maintained, the volumetric flow will be the same in each section enabling us to predict the expected and the measured flow in each test sections. This will be used to initially calibrate and later verify the functioning of the sensors.

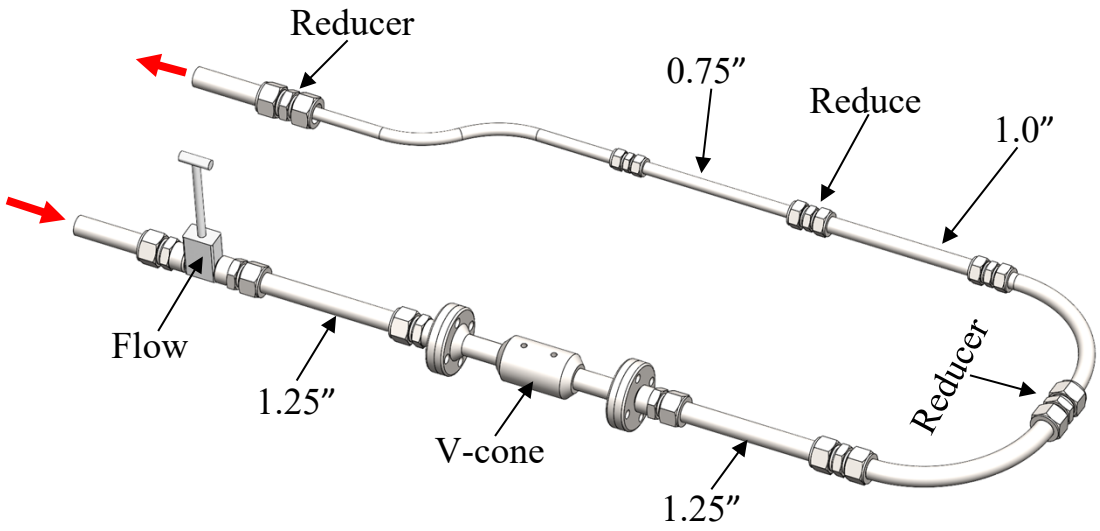

Figure 8. Three test sections for the mercury flow sensor

The ECFM set-up is placed inside TTF [7] where the Gas Wall experiment was conducted. Both the inlet and the outlet tap for the Gas wall experiment will remain in place, but the flow sensor test section will be added. Fig. 9 shows an image of the TTF loop after installation.

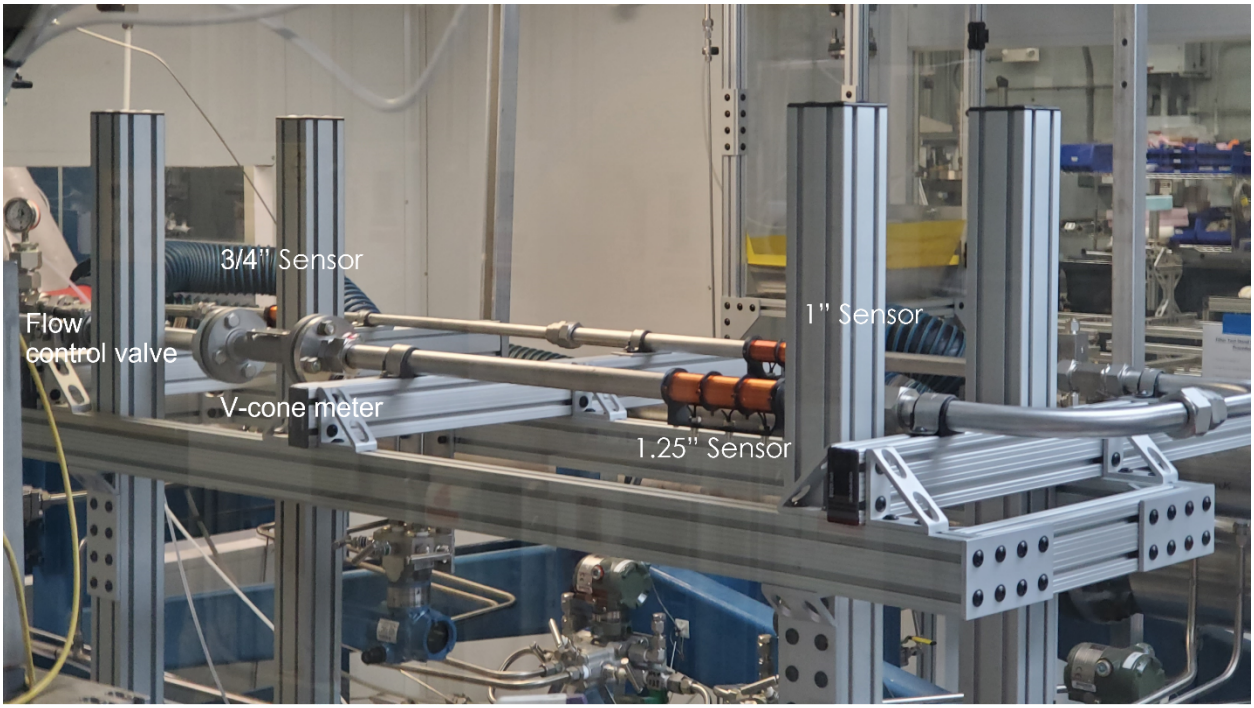

Figure 9. Location of the ECFM inside TTF

Parameter	Parameter Range
Pipe material	316L stainless steel
Liquid metal material	Mercury
Liquid metal volumetric flow	Up to 9.1 GPM
Bobbin geometry	3 bobbins varying in number of coils and diameter
Excited AC amplitude	Up to 0.25 A
Excited AC frequency	100 to 20000 Hz

Table 3. List of parameters varied in this experimental setup for the liquid mercury experiments.

The details of the experiment are shown in Table 3. The liquid volumetric flow rate and excited AC frequency were scanned for all three bobbins. The coil gauge diameter of the secondary coil was also modified for bobbin #5. Number of coils also differ for each bobbin. The details of the bobbin are shown in Table 4.

Parameter	Bobbin #4	Bobbin #5	Bobbin #6
Bobbin axial coil spacing	2.54 mm	.54 mm	2.54 mm
Bobbin radial thickness	2.54 mm	2.54 mm	2.54 mm
Bobbin axial coil width	50.8 mm	50.8 mm	50.8 mm
Bobbin coil gauge diameter (P,S)	0.452, 0.452 mm	0.452, 0.255 mm	0.452, 0.452 mm
Number of coil turns in each coil	1	1	1
Number of coils in (S,P,S) coils	100,100,100	147,100,147	100,98,100

Table 4. Geometry of the bobbin for the liquid mercury experiments.

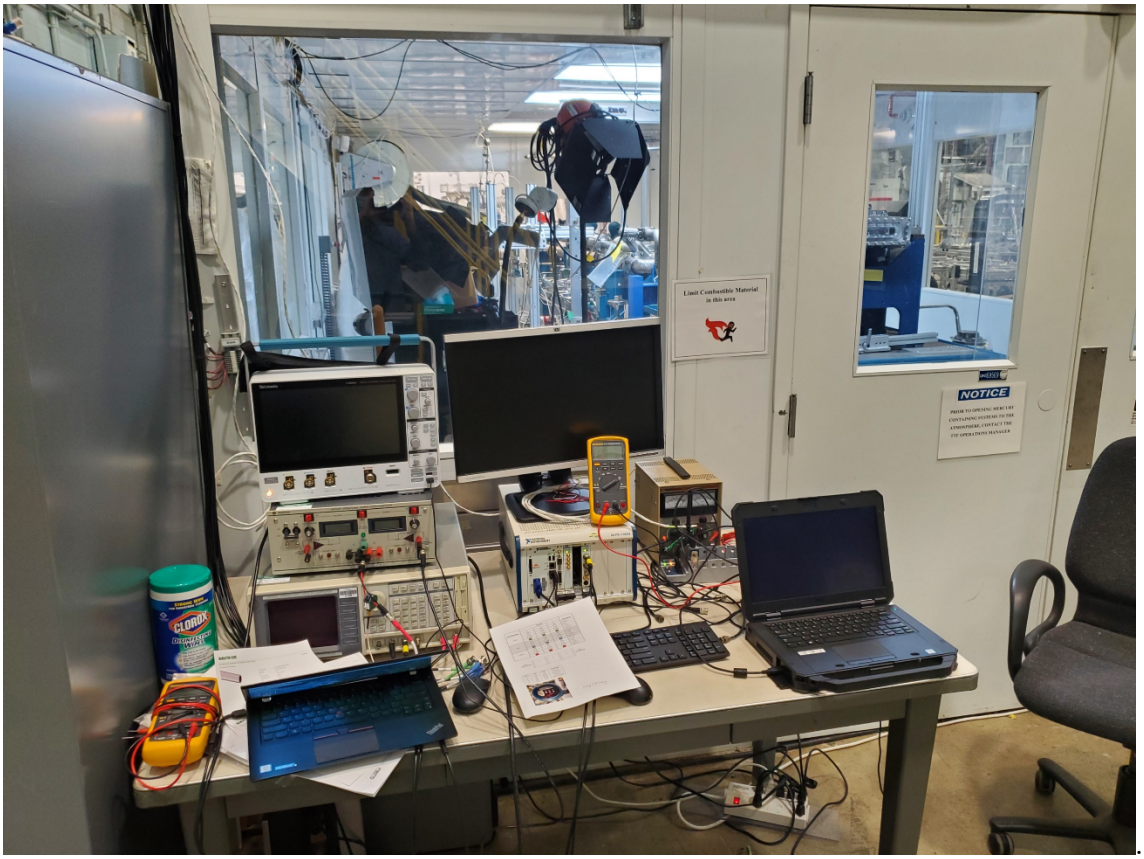

Figure 10. Image of the ECFM experimental setup outside the TTF enclosure.

The ECFM electronics and the data acquisition system is placed outside the TTF enclosure. This is shown in Fig. 10. Most of this ECFM electronics setup is similar to the dry rod experimental setup shown in Fig. 3, so only the differences are highlighted here. An oscilloscope is used to measure the current instead of the multimeter. It was found that the multimeter did not function above 5000 Hz. Instead of using 40 dB gain on the lock-in amplifier, only 30 dB gain was used here to fit within the voltage range of the PXI digitizer While this is sufficient for the dry rod experiments, the multimeter is not sufficient for the liquid mercury experiments. Another difference is that Pearson probes were not wired to the output of the lock-in amplifier. They were found to be unnecessary, and a direct voltage measurement, therefore, was used for the liquid mercury experiments. The volumetric flow output of the v-cone flow meter goes to a transmitter and flow computer, which outputs a current signal. This is measured by a multimeter.

The data analysis for the liquid mercury experiment was simpler than the dry rod experiment. Because the bobbin was stationary in these experiments, there was no need to do a forward and backward measurement. A direct voltage measurement was used so there was no need to measure the impedance with an impedance meter. A zero-velocity calibration is done here for stagnant liquid mercury flow. This is subtracted from the measurement at a constant non-zero flow velocity. The square root of the sum of the square of the calibrated in-phase and quadrature signal is the measured experiment AC current, $\tilde{I}_{exp}$.

Another difference between the dry solid rod and liquid mercury experiment was the large importance of "non-flow" components[8] that can cause a systematic error in the ECFM measurement. Drifts in the "non-flow" components can compromise the accuracy of the measurement because the ECFM technique requires a zero-velocity calibration. This is especially problematic if the "non-flow" component is substantially larger than the flow component. An example of this is shown in Fig. 11 for the sensitivity /

"non-flow" component of bobbins #4 to #6. The flow / "non-flow" component can be very small, ranging for 10^{-1} to 10^{-3}. This ratio becomes smaller at larger frequencies. For the dry rod test where the maximum frequency was 1000 Hz, this was not a significant issue. For higher frequencies used in the liquid mercury experiments up to 20000 Hz, this ratio can be much smaller.

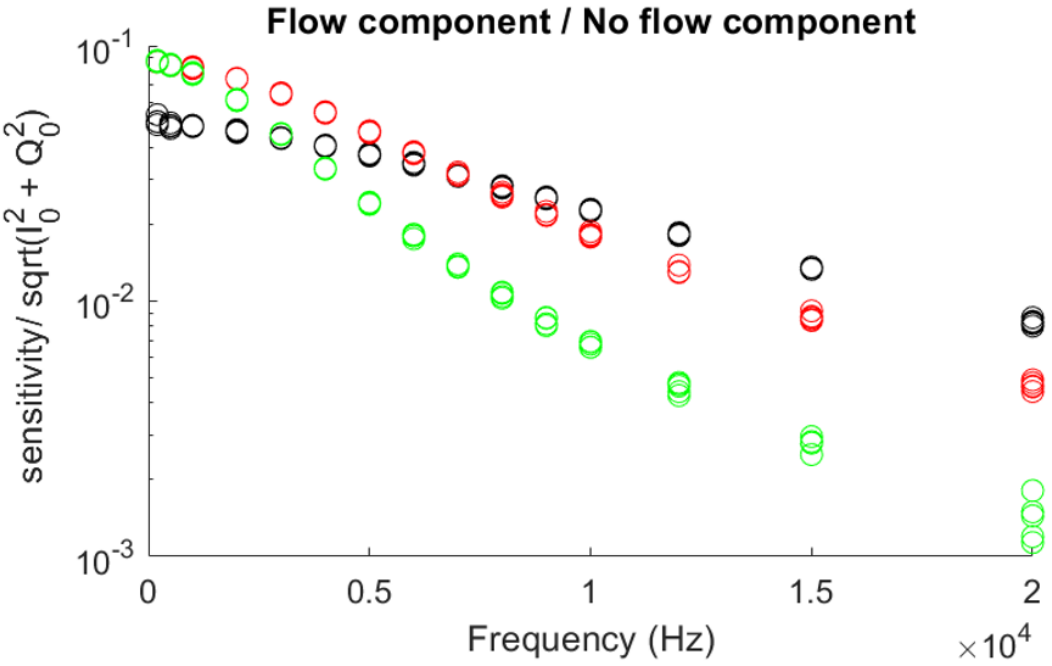

Figure 11. Flow/ "non-flow" component for bobbin #4 (black), bobbin #5 (red), and bobbin #6 (green).

Unfortunately, drifts can occur in the "non-flow" component. Fig. 12 shows an example of these drifts for bobbin #4 at 20000 Hz. Data was taken every minute for the in-phase component for bobbin #4 for 15 minutes. A small, but clear drift is observed. It should be noted that this drift is only 0.06 V out of 37 mV. However, at 20000 Hz, the flow component is only a small fraction of the non-flow component, this can be a serious error. This error likely results from temperature changes in liquid mercury and/or bobbin that can modify material properties such as electrical conductivity. Correction for this error will require thermocouples, which were not available for this experiment. These drifts were empirically minimized in experiments by turning the power supply on and off to maintain similar temperatures and by taking zero velocity calibrations routinely between measurements. Experiments are repeated multiple times at each data point to estimate systematic errors due to these drifts.

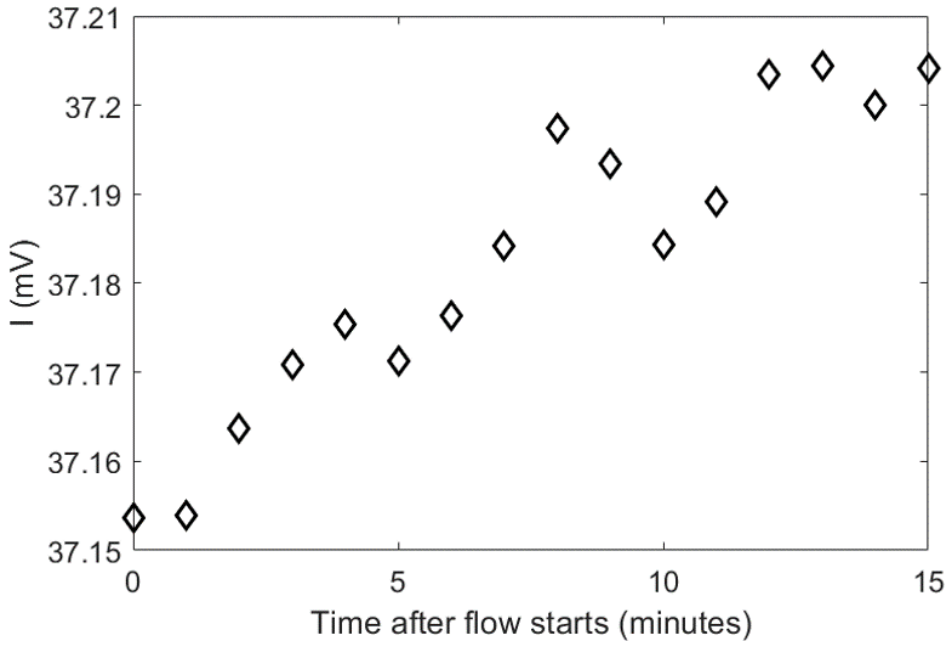

Figure 12. Data was taken every minute for the in-phase component for bobbin #4.

3.2 ECFM Modeling Setup and Procedure

For modeling the electromagnetic response of the ECFM sensor in both a solid rod and liquid mercury, COMSOL Multiphysics[6] is used to model the sensitivity of the ECFM with realistic geometry. This is accomplished using the magnetic and electric fields interface within the AC/DC module to solve Eq. (2). Since the geometry is axisymmetric, the model is also 2-D axisymmetric. For the solid rod modeling, a velocity is imposed within the AC/DC module. For the liquid mercury modeling, a velocity profile input is required. This is done using computational fluid dynamics modeling.

3.2.1 ECFM Modeling Setup and Procedure for Solid Rod

The simulation geometry for the ECFM sensor is shown in Fig. 13a). Fig. 13b) is an expanded view of Fig. 13a) near the bobbin. The domains consist of an infinite layer, air, copper coils, acetal plastic bobbin, PVC pipe, air gap between the conducting medium and bobbin, and solid simulation rod that can either be 316 SS or aluminum. The important lengths of various dimensions used in the inputs are discussed in Section 3.1.1. Material properties such as electrical conductivity, permittivity, and magnetic permeability are provided either by manufacturers or estimated from COMSOL material library. The relative magnetic permeability is assumed to be 1 for all materials. The electrical conductivity for the copper coils, aluminum rod, and 316 SS rod are 5.96×10^7, 2.46×10^7, and 1.35×10^6 S/m, respectively. Acetal plastic, a dielectric used as material for the bobbin, is assumed to have a permittivity equal to 3.7. The PVC pipe is assumed to have a permittivity equal to 3.4.

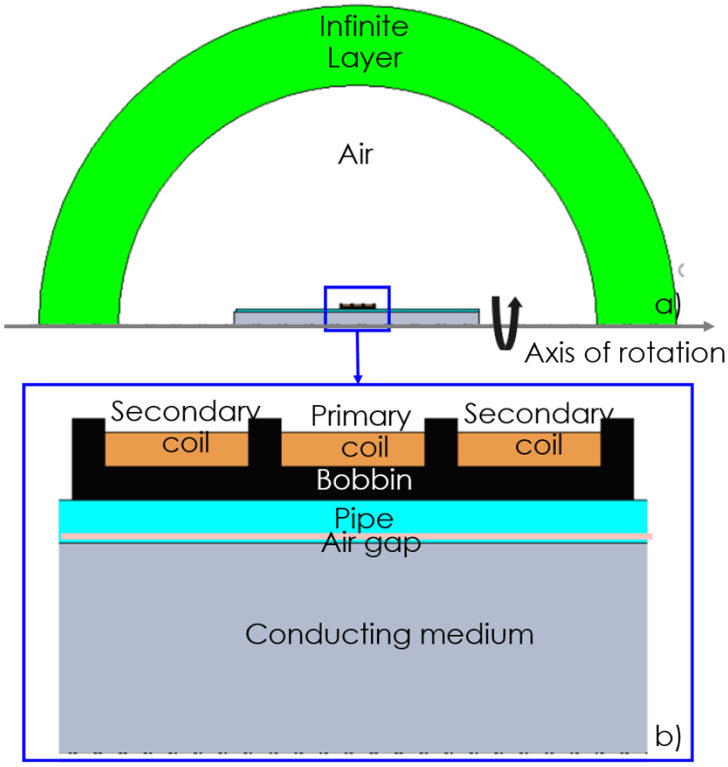

Figure 13. COMSOL modeling setup for ECFM sensor.

To model an infinite problem with open boundaries in a finite computational domain, a semicircle infinite element layer is used as an artificial absorbing layer that should nominally absorb outgoing waves without reflecting them back into the interior. Magnetic insulation boundary conditions are used at the exterior boundary. The AC current and frequency is excited at the primary coil. No power is excited at the secondary coils and these coils are assumed to be part of a receiving electrical circuit with resistance and inductance measured by the signal impedance analyzer in Fig. 6. An axial velocity of constant velocity is specified for the conducting medium, pipe and air gap. This is equivalent simulation setup, but in a different reference frame, to the actual experiment where the bobbin is moved but the simulation rod and pipe are stationary. The only difference in the result is that the sign of the sensitivity is reversed.

The sensitivity is then calculated by the difference of the electric potentials in each of the two secondary coils. Using the experimentally measured impedance at the secondary coils, the sensitivity can be related to the AC current sensitivity measurement. Because of the potential asymmetry in the number of coils in each of the secondary coil, the modelled sensitivity can also be non-zero when the velocity is zero. Therefore, similar to the experimental procedure, the sensitivity for a non-zero velocity case is subtracted from the sensitivity in a zero-velocity case before being compared to the experiments.

An example result for the amplitude of the AC magnetic field is shown in Fig. 14 for a case with rod velocity = 0.5 m/s, rod material = aluminum, AC frequency = 250 Hz, AC current amplitude = 0.5 A. It is easily observable that the AC magnetic field amplitude is large at locations that are both radially and axially near the primary coil. The AC magnetic field is negligible at distances far away from the primary coil. This provides strong confidence that a finite computational domain is reasonable. While not shown, both mesh convergence and geometry convergence of the thickness of the semicircle infinite element layer has been verified. Each case can be solved numerically on a standard laptop with 16 GB memory in less than a minute.

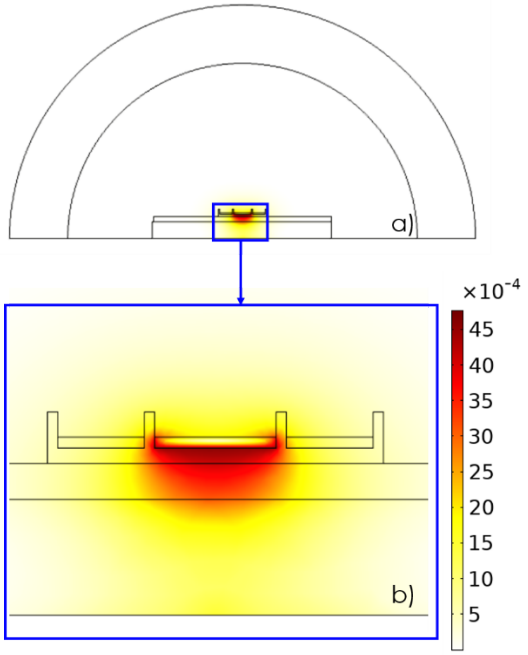

Fig. 14. AC magnetic field (T) for case with rod velocity = 0.5 m/s, rod material = aluminum, AC frequency = 250 Hz and AC current amplitude = 0.5 A.

3.2.2 ECFM Modeling Setup and Procedure for Liquid Mercury

The modeling setup for liquid mercury is similar to the solid rod case in Fig. 13 in section 3.2.1. Only the differences are noted here. In terms of the domain and materials, the solid rod in Fig. 10 is now assumed to be liquid mercury, with an electrical conductivity of 1.092×10^6 S/m, instead of 6061-T6 aluminum. The pipe is now assumed to be 316 SS with an electrical conductivity of 1.35×10^6 S/m instead of PVC plastic. The 316 SS pipe dimensions are chosen to match the experiment with an outer diameter of 19.05 mm, 25.4 mm, and 31.75 mm with a thickness of 1.651, 2.11, 3.05 mm, respectively. The air gap is assumed to be negligible and equal to 0 m. The dimensions are chosen from a segment of the experimental setup discussed in Section 3.1.2 where the bobbin is centered on a 0.61 m length liquid mercury domain. The relative magnetic permeability for all materials is assumed to be 1.

Instead of applying an imposed velocity to the solid rod, PVC pipe, and air gap in the solid rod case, the velocity is now applied only to the liquid mercury. This velocity comes from computational fluid dynamics modeling.

3.2.3 Computational fluid dynamics modeling

SolidWorks flow simulation is used for 3-D computational fluid dynamics modeling using the 3-D drawing shown in Fig. 8 as input. All tubes and fittings are modeled as 316 stainless steel. No surface roughness is assumed for all flow channels. Room temperature of 20°C is used for all solids and liquids. An outlet boundary condition of 1 atmosphere pressure is assumed. The inlet boundary condition is the volumetric flow rate, which depends on the conditions of the experiment. The material properties used for 316 stainless steel and liquid mercury are shown below in Table 5.

	Liquid mercury	316 Stainless Steel
Mass Density	13580 [kg/m^3]	7990[kg/m^3]
Heat capacity	139 [J/(kg*K)]	500[J/(kg*K)]
Thermal conductivity	8.70 [W/(m*K)]	1630[W/(m*K)]
Dynamic viscosity	.00155 [Pa*s]	

Table 5. Material properties used in the computational fluid dynamics model.

SolidWorks solves the Navier Stokes equation for mass, momentum, and energy conservation laws. Depending on the Reynold's number, either laminar or turbulent flow is considered. The Reynold's number in a circular pipe is $\rho QD/\mu A$ where ρ is the mass density of the fluid, Q is the volumetric flow rate, D is the inner diameter of the pipe, μ is the dynamic viscosity of the fluid, and A is the cross sectional area. For all three pipe diameters and volumetric flow rates > 0.045 kg/sec the Reynold's number > 10^4. Given that the critical Reynolds number is 2900 for the flow to transition from Laminar to fully turbulent, a turbulent model is used in these simulations. A modified k-epsilon model with damping functions proposed by Lam and Bremhorst [9]is used at the turbulence model. No-slip boundary conditions are assumed.

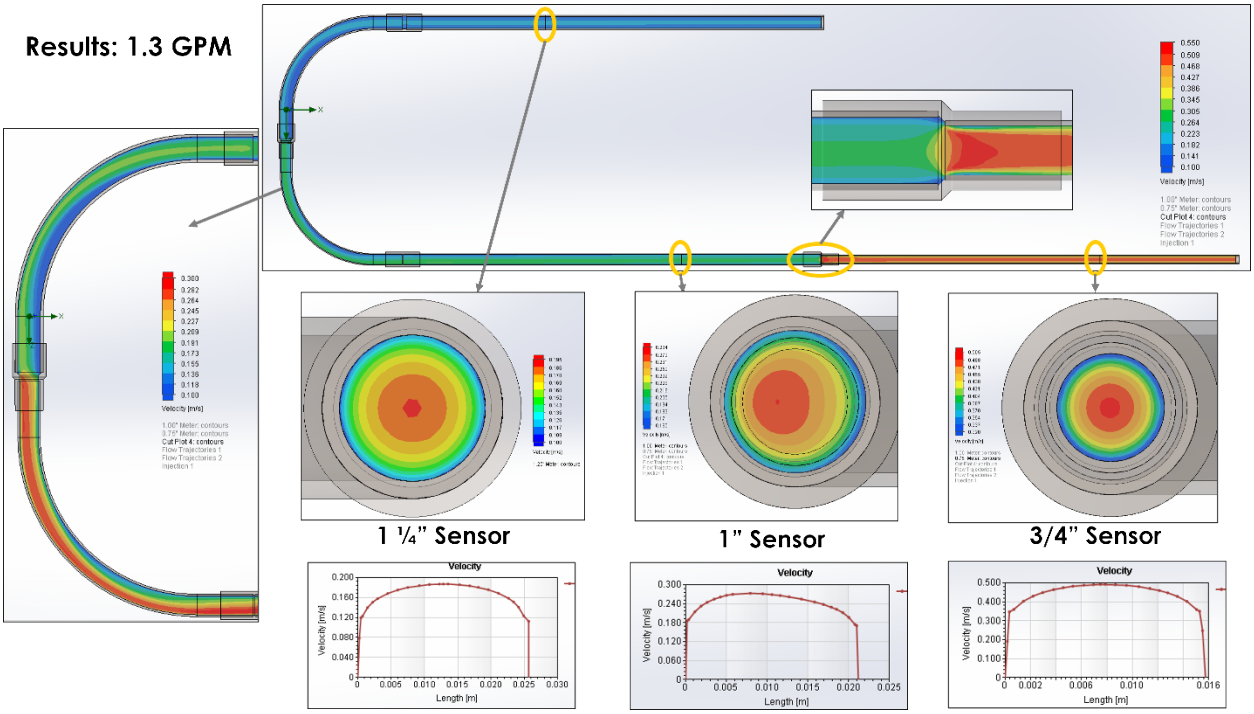

Figure 15. Image of the 3-D computational fluid dynamics results for the ECFM setup shown in Fig. 9. The volumetric flow input used is 1.3 GPM.

An image of the 3-D results are shown in Figs. 15, 16, and 17 for volumetric flow input of 0.0585, 0.216, and 0.41 kg/s. The flow at the 31.75 and 19.05 mm sensors are relatively circular symmetric for all flow rates. The flow profile also appears to similar for the three flow rates. The flow profile is clearly not parabolic and is representative of turbulent flow. One interesting point is that the 1" sensor shows some asymmetry after the 180° bend. The 180° bend appears to disrupt the flow and fully developed flow is not achieved at the 1" sensor. Given that the electromagnetic model is 2-D axisymmetric, an average over the ¾, 1, and 1.25" cross section of the computational fluid dynamic results is used as inputs into the 2-D electromagnetic model.

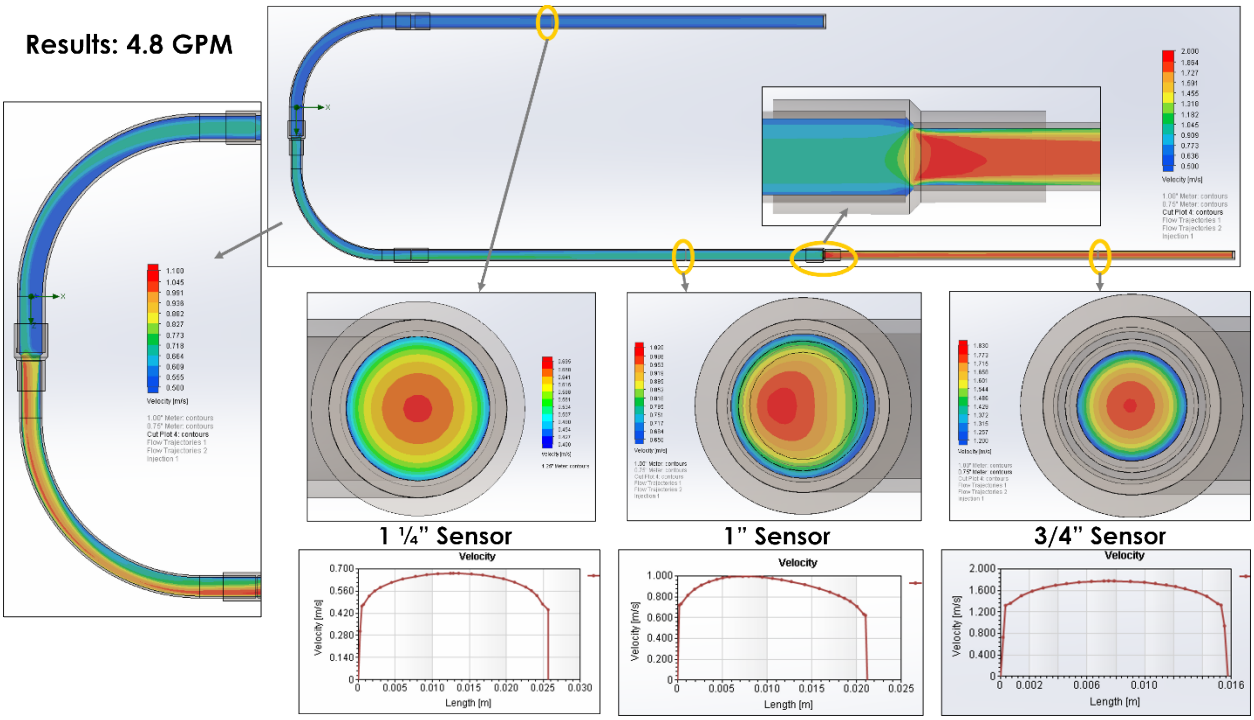

Figure 16. Image of the 3-D computational fluid dynamics results for the ECFM setup shown in Fig. 9. The volumetric flow input used is 4.8 GPM.

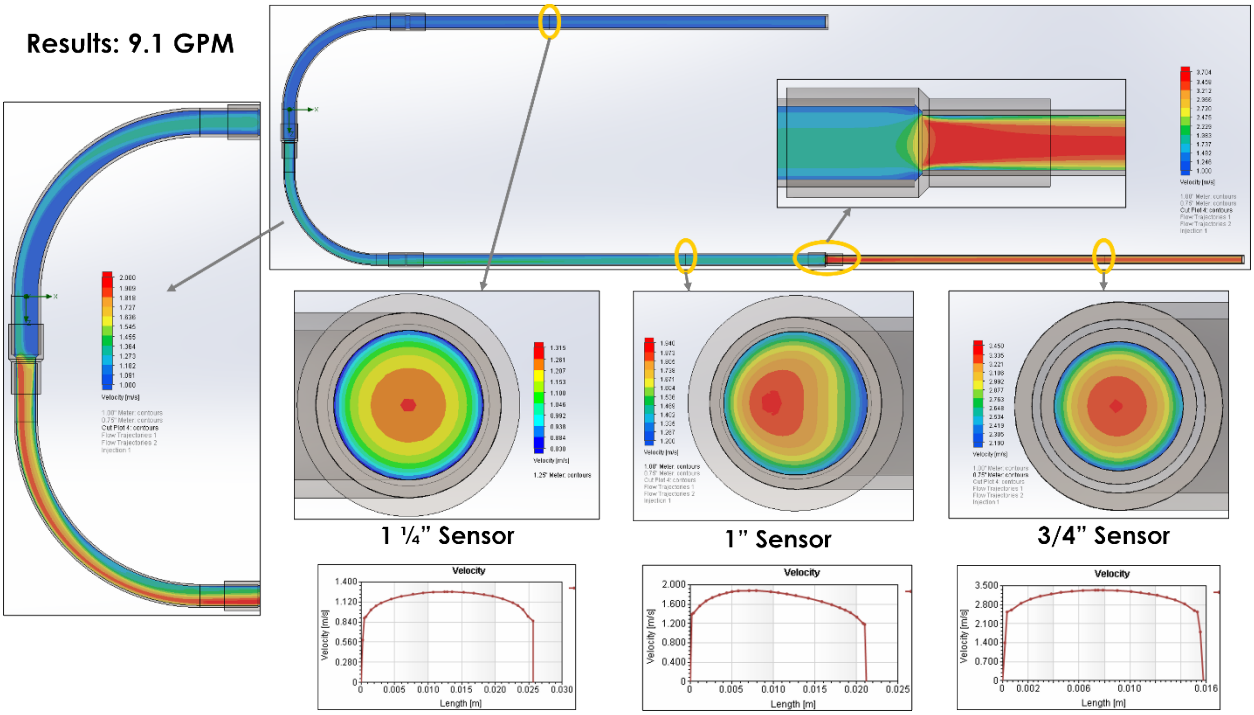

Figure 17. Image of the 3-D computational fluid dynamics results for the ECFM setup shown in Fig. 9. The volumetric flow input used is 9.1 GPM.

4. RESULTS

4.1 Experimental and Modeling Results for Solid Rod

The experimental and modeling results are shown for parametric scans of excited current, frequency, velocity of the bobbin, bobbin geometry, and different solid rod material. The experimental results are shown in the symbols and the modeling results are shown in the lines in the figures in this subsection. The agreement is excellent in all cases. The normalized root mean square error (NRMSE) for all the parametric scans are less than 10%.

Fig. 18 shows the results for a frequency scan at three different velocities equal to 0.1, 0.3, and 0.5 m/s for the case with an aluminum rod, PVC pipe and 0.5 A excited current. As seen in the Fig. 18, the experimental and simulation results agree remarkably in both the magnitude and trend. The trend with frequency is due to the effect of the skin depth compared to the radius of the conducting medium that was discussed in previous sections. At low frequencies, the skin depth is much larger than the radius of the rod and the ECFM sensor is less sensitive to the velocity of the rod. At high frequencies, the skin depth is much smaller than the radius of the rod and the ECFM sensor is again not sensitive to the radius of the rod. The sensitivity appears to peak at a frequency when the skin depth is on the order of half the radius of the rod. The NRMSE for the frequency scan at velocities equal to 0.1, 0.3, and 0.5 m/s are 5.5%, 4.5%, and 3.8%. It is likely that the NRMSE is lowest at 0.5 m/s due to better signal to noise.

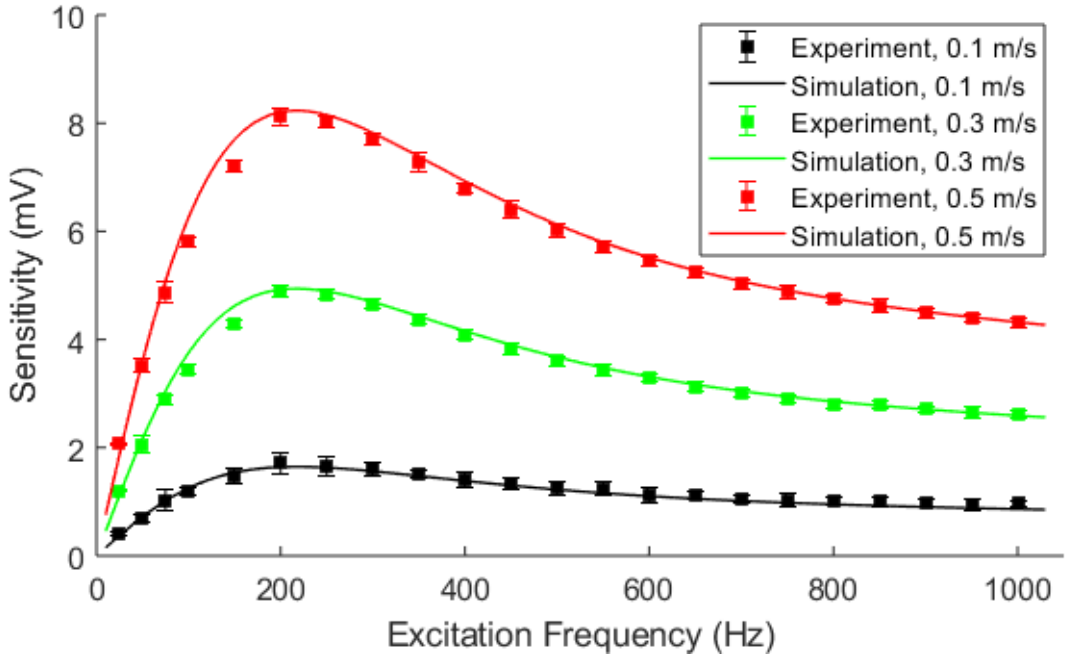

Figure 18. Experimental and simulation results for a frequency scan with an aluminum rod, PVC pipe, 0.5 A excited current, and bobbin #3 for velocities = 0.1, 0.3, and 0.5 m/s.

Fig. 19 shows the results for a velocity scan at three different frequencies of 50, 200, and 600 Hz for the case with an aluminum rod, PVC pipe, bobbin#3 and current of 500 mA. As seen in Fig. 19, the experimental and simulation results agree remarkably in both the magnitude and trend. The trend is linear in both experiment and modeling, as expected for a velocity scan. The NRMSE is 1.7%, 2.4%, and 2.1% for the 50, 200, and 600 Hz cases.

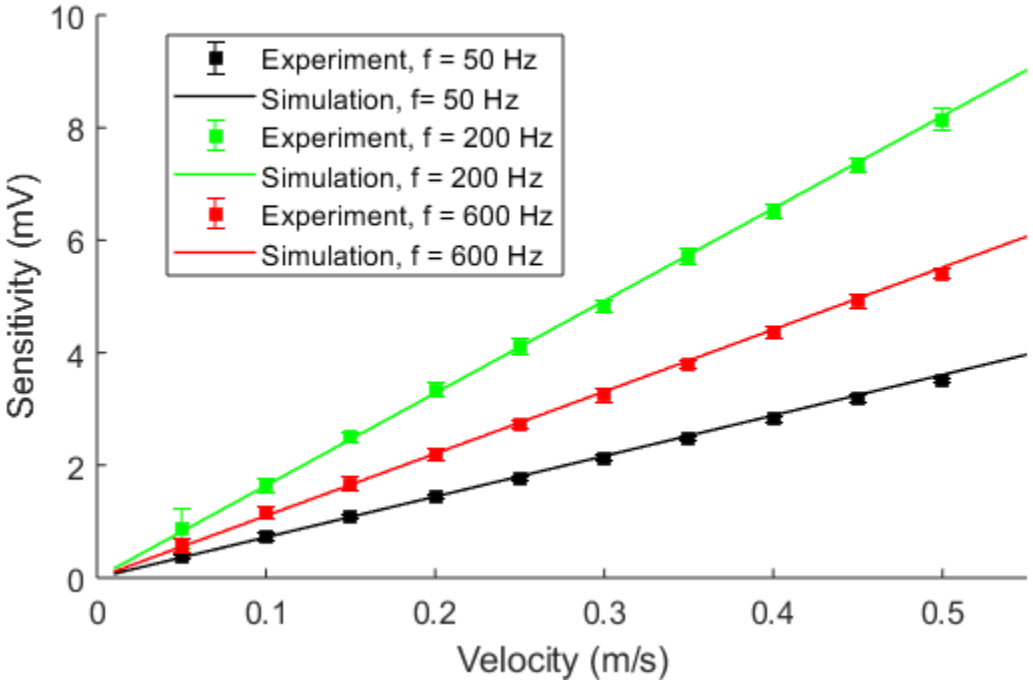

Figure 19. Experimental and simulation results for a velocity scan with an aluminum rod, PVC pipe, 0.5 A excited current, and bobbin #3 for frequencies = 50, 200, and 600 Hz.

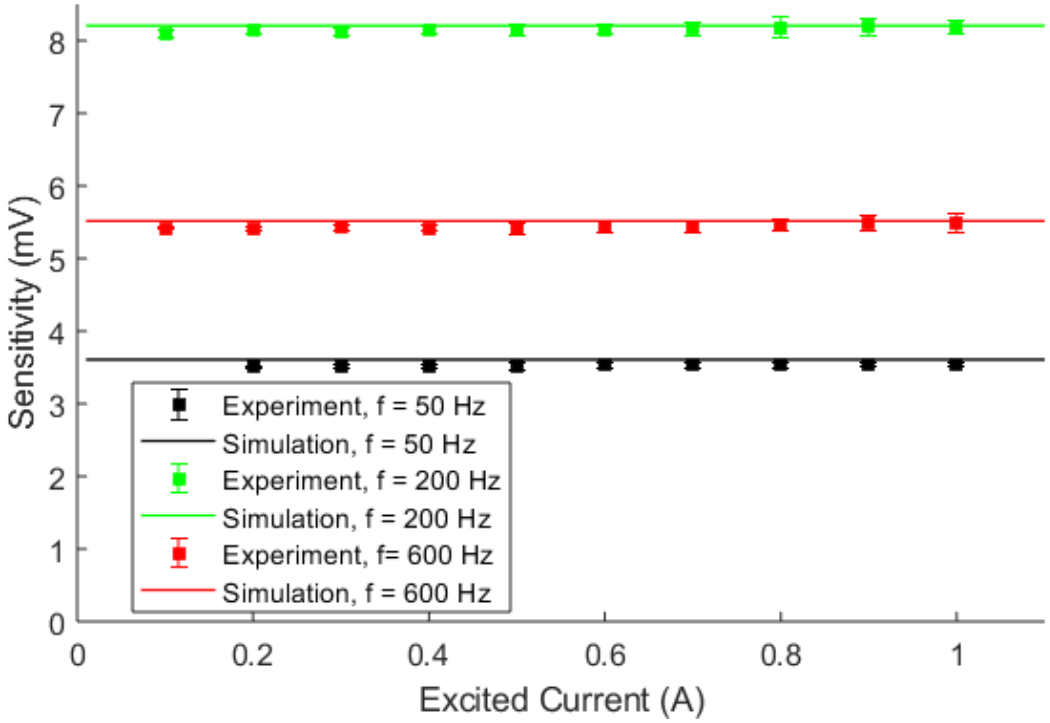

Figure 20. Experimental and simulation results for a current scan with an aluminum rod, PVC pipe, 0.5 A excited current, and bobbin #3 for frequencies = 50, 200, and 600 Hz.

Fig. 20 shows the results for an excited current scan at three different frequencies of 50, 200, and 600 Hz for the case with an aluminum rod, PVC pipe, bobbin#3 and velocity of 0.5 m/s. As seen in Fig. 18, the

experimental and simulation results agree remarkably in both the magnitude and trend. Because the sensitivity is normalized to the excited current, it is expected that the sensitivity does not depend on the excited current. The trend is therefore flat in both experiment and modeling as expected. The NRMSE is 2.4%, 0.7%, and 1.5% for the 50, 200, and 600 Hz cases.

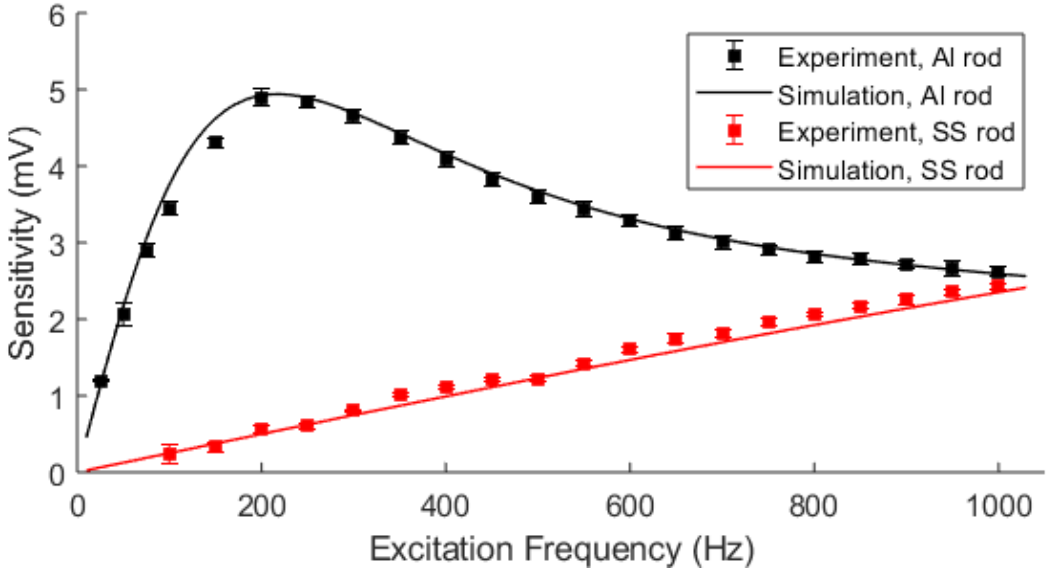

Figure 21. Experimental and simulation results for a frequency scan with a PVC pipe, 0.5 A excited current, bobbin #3, and velocity = 0.3 m/s for a 316 SS and aluminum rod.

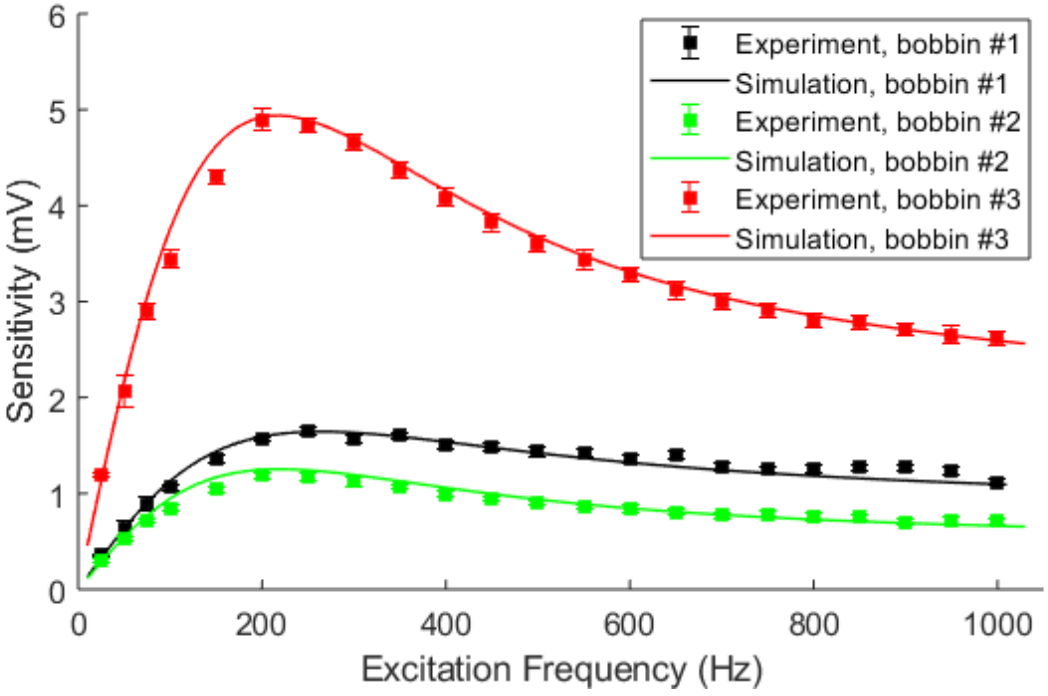

Figure 22. Experimental and simulation results for a frequency scan with a PVC pipe, 0.5 A excited current, aluminum rod, and velocity = 0.3 m/s for bobbins #1, #2, and #3.

Fig. 21 shows the results for experimental and simulation results for a frequency scan with a PVC pipe, 0.5 A excited current, bobbin #3, and velocity = 0.3 m/s for a 316 SS and aluminum rod. The experimental and simulation results agree well in both magnitude and trend. The response to the aluminum and SS rod is very different. This is again because of the skin depth effect due to the factor of ~ 20 difference between electrical conductivities between Al and SS. Assuming the sensitivity appears to peak at a frequency when the skin depth is on the order of half the radius of the rod as in Fig. 19, the peak for the 316 SS case should be at ~ 4000 Hz. The NRMSE is 4.5% and 7.8% for the Al and SS cases.

Fig. 22 shows the results for experimental and simulation results for a frequency scan with a PVC pipe, 0.5 A excited current, aluminum rod, and velocity = 0.3 m/s for bobbins #1, #2, and #3. The experimental and simulation results agree well in both magnitude and trend. The bobbins differ in number of coils and axial coil width. This suggests that geometry is important and that a finite element model can capture the effects of geometry on sensitivity. The NRMSE is 5.5% , 6.7%, and 4.5% for bobbin #1, #2, and #3 cases.

In summary, the ECFM response for variations in rod velocity, rod conductivity, excited frequency, excited current, bobbin coil length, and number of coils were measured and compared with simulation. For all parametric scans, the agreement between experiment and modeling was very good with a normalized root mean square error of less than 10%. This is very encouraging validation of the COMSOL model and suggests that COMSOL can be used to predict ECFM response in more complicated experimental setups in the future.

4.2 Experimental and Modeling Results for Liquid Mercury

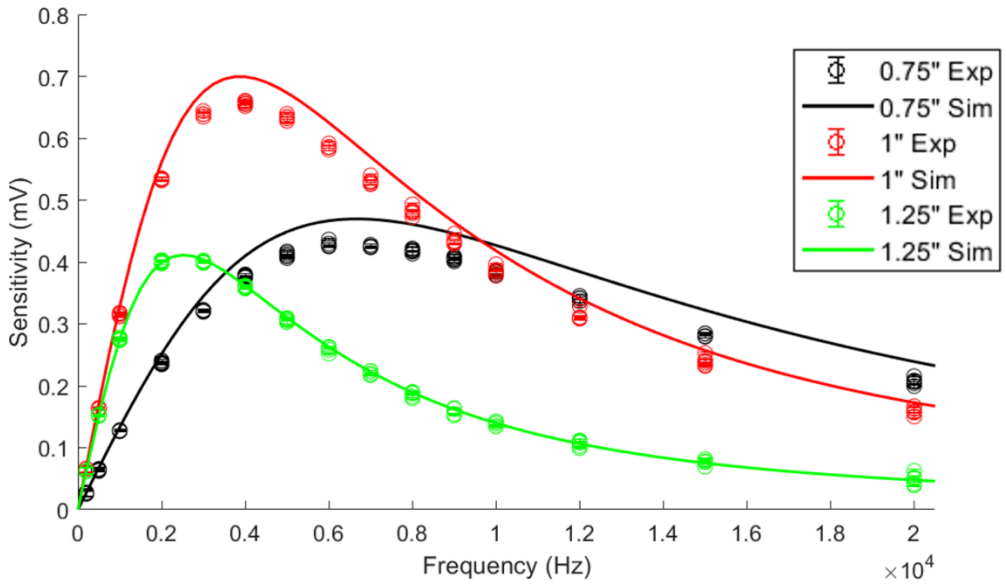

Figure 23. Experimental and modeling results for sensitivity for a frequency scan for bobbins #1 to #3. The volumetric flow input was 9.1 GPM.

Figure 23 shows the results between experiments and modeling for the TTF liquid mercury loop. This is done at a volumetric flow rate of 9.1 GPM for a frequency scan from 100 to 20000 Hz for bobbins #1 to #3. The measurement was repeated 5 times at each data point. The agreement between experiment and modeling is good for both magnitude and trend. The sensitivity peaks at different frequencies because the diameter of the pipes and bobbins differ. The sensitivity peaks when the skin depth is approximately half of the pipe radius. Since the skin depth depends on the frequency, the sensitivity peaks at different

frequencies. The normalized root mean square error is 8.9%, 6.5%, and 5.2% for bobbins #1 to #3 respectively.

Figure 24 shows the results at different flow rates and various frequencies for bobbin #2. The measurement was repeated 5 times at each data point. Again, experiments and modeling agree well in both magnitude and trend. The sensitivity is linear to the flow. This is expected because the Reynolds number > critical Reynolds number, so the flow is very turbulent in all cases. The NRMSE is less than 10% for all these cases.

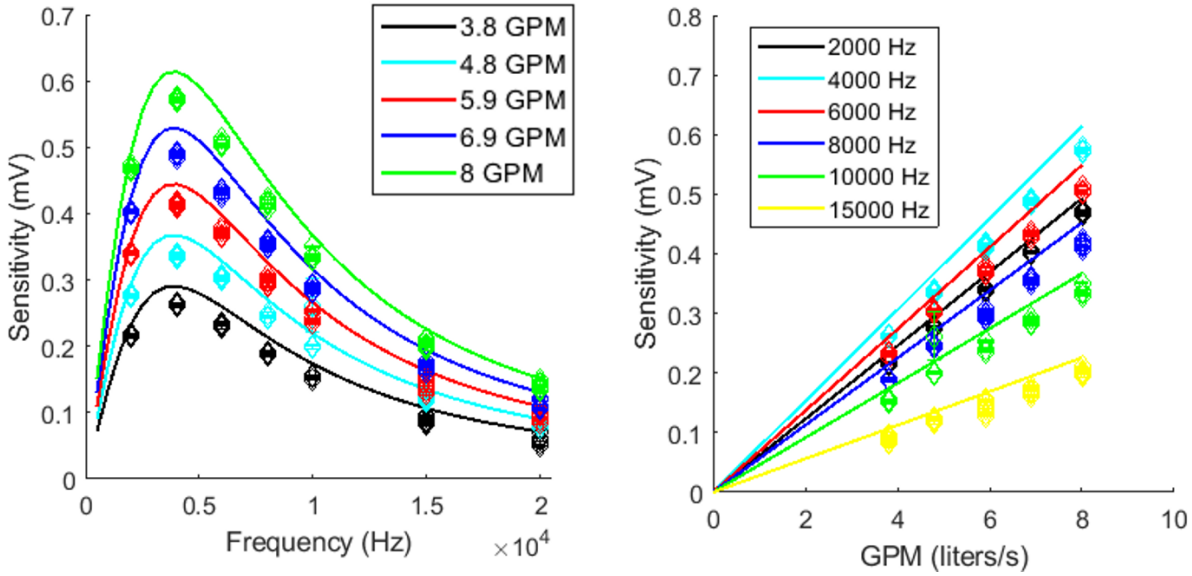

Figure 24. Left. Experimental and modeling results for sensitivity for a frequency scan for bobbins #2 at different input volumetric flow rates. Right. Experimental and modeling results for sensitivity for a volumetric flow rate scan for bobbin #2 at different frequencies.

4.3 Proof of principle velocity profile calculation using and ECFM measurement at multiple frequencies and COMSOL electromagnetic modeling

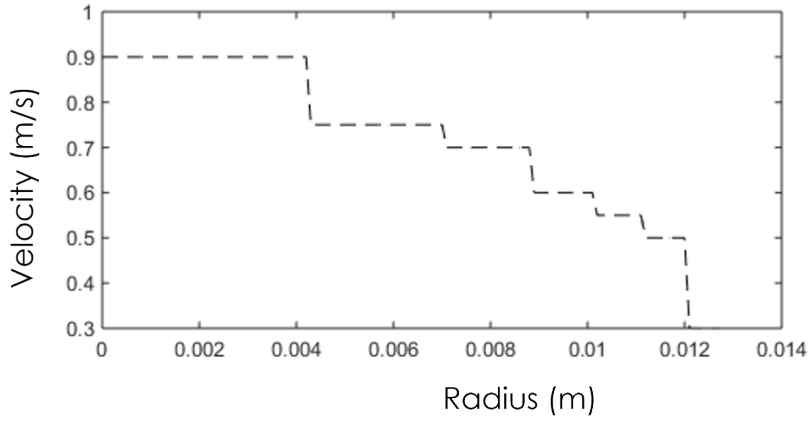

Fig. 25. Example sum of 6 rectangular functions as velocity profile.

The ECFM sensor measures the sensitivity to infer the velocity. The COMSOL model simulates the sensitivity for a given velocity profile. For multiple frequency measurements, it can be hypothesized that

not only can the ECFM sensor measure the velocity, but it may also measure the velocity profile. This has not been demonstrated before and this section outlines a mathematical method that can be used to do so.

Assuming the velocity radial profile is sum of N rectangular functions and sensitivity is linearly proportional to the velocity at each Heaviside function, a COMSOL electromagnetic simulation from i = 1 to N Heaviside functions are used to calculate to the sensitivity for M frequencies. This results in a linear algebra problem $\overleftrightarrow{A} \cdot \vec{v} = \vec{b}$ where $\overleftrightarrow{A}$ is a M x N matrix that converts velocities to sensitivities, $\vec{v}$ is a 1 x N vector of velocities and $\vec{b}$ is a M x 1 vector of sensitivities. An example sum of N rectangular functions is shown in Fig. 25 for N = 6. $\overleftrightarrow{A}$ is calculated from the COMSOL electromagnetic simulations, $\vec{b}$ is measured using the ECFM measurements at multiple frequencies, and $\vec{v}$ is unknown to be inferred from the combined measurement and model.

Mathematically, this is a standard minimization problem to find the minimum of $\left|\overleftrightarrow{A}\vec{v} - \vec{b}\right|$ for the given measurements of $\vec{b}$. There are many potential ways to solve this, but what is chosen here is to use simulated annealing for the example case in Fig. 18 for velocity of a solid rod at v = 0.3 m/s and v = 0.5 m/s. , $\vec{b}$ contains all 22 measured sensitivities at the appropriate frequencies. $\overleftrightarrow{A}$ is calculated from the COMSOL electromagnetic model. The initial guess for each of the N = 7 inputs of the simulated annealing is assumed to be a random number chosen from a uniform distribution from 0 to 1. The results are shown in Fig. 26 for the inferred velocity profile in the black and red symbols. This compares favorably to the known velocity from the solid rod experiments.

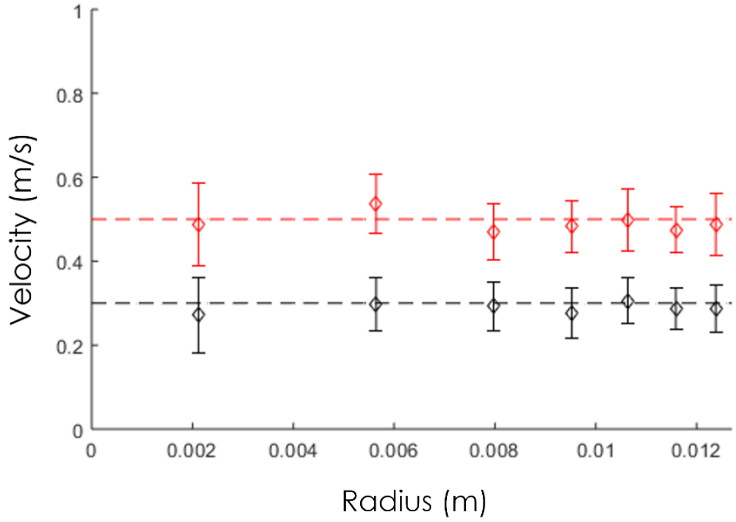

Fig. 26. Inferred velocity profile from simulated annealing. Black and red symbols are the inferred velocity form v = 0.3 and 0.5 m/s. Black and red dashed lines are the known velocity profile from the moving solid rod.

5. CONCLUSION AND FUTURE WORK

This report summarizes the recent results of the ECFM sensors. Both experimental and modeling results are presented for the ECFM sensor in a dry conducting rod experiment. Excellent agreement between experiment and modeling is shown for a wide range of parameters in the solid rod experiments. This provides confidence that a validated model for the ECFM sensor has been developed. This model has then been used to predict the sensitivity of the ECFM sensor in the TTF liquid mercury experiment. Excellent agreement is again confirmed between experiment and simulation.

Future work could include multiple aspects. From a measurement viewpoint, adding a temperature sensor to calibrate the zero-velocity drift could greatly improve the measurement accuracy and ensure a real time calibration. This will particularly be important for future liquid lead and liquid sodium measurements. From a modeling viewpoint, it would be useful to apply the velocity profile calculation technique for liquid metals where the flow profile is non-uniform.

6. ACKNOWLEDGEMENTS

This work was funded by the DOE Office of Nuclear Energy (NE) Versatile Test Reactor (VTR) Project. The reported work resulted from studies that support a VTR conceptual design, cost, and schedule estimates for DOE-NE to make a decision of procurement. As such, it is preliminary.

7. REFERENCES

[1] J. Brewer, R. Jaross, R. B.-I. T. on Nuclear, and undefined 1971, "Eddy-current probe-type sodium flowsensor for FFTF reactor fuel channel flow monitoring," *ieeexplore.ieee.org*, Accessed: Jul. 08, 2021. [Online]. Available: https://ieeexplore.ieee.org/abstract/document/4325894/

[2] P. A. Davidson and E. v. Belova, " An Introduction to Magnetohydrodynamics ," *American Journal of Physics*, vol. 70, no. 7, pp. 781–781, Jul. 2002, doi: 10.1119/1.1482065.

[3] S. M. Cetiner, K. M. Oleksak, R. J. B. Warmack, M. J. Roberts, M. N. Ericson, and A. Fathy, "Preliminary Design Study for an Eddy Current Flow Meter for the Versatile Test Reactor," 2019, Accessed: Jul. 08, 2021. [Online]. Available: http://www.osti.gov/contact.html

[4] S. Poornapushpakala, C. Gomathy, J. I. Sylvia, B. Krishnakumar, and P. Kalyanasundaram, "An analysis on eddy current flowmeter - A review," *Proceedings of the International Conference on "Recent Advances in Space Technology Services and Climate Change - 2010", RSTS and CC-2010*, pp. 185–188, 2010, doi: 10.1109/RSTSCC.2010.5712844.

[5] D. Nielsen, D. Polzin, R. Omberg, and B. Makenas, "Eddy Current Flow Measurements in the FFTF," 2017, Accessed: Jul. 08, 2021. [Online]. Available: https://www.osti.gov/biblio/1406803

[6] AB COMSOL, "COMSOL Multiphysics User Guide."

[7] P. Spampinato, V. Graves, and S. Schrock, "SNS Target Test Facility for remote handling design and verification," 1998, Accessed: Jul. 08, 2021. [Online]. Available: https://www.osti.gov/biblio/291077

[8] D. Nielsen, D. Polzin, R. Omberg, and B. Makenas, "Eddy Current Flow Measurements in the FFTF," 2017, Accessed: Oct. 06, 2021. [Online]. Available: https://www.osti.gov/biblio/1406803

[9] C. K. G. Lam and K. Bremhorst, "A Modified Form of the k-ε Model for Predicting Wall Turbulence," *Journal of Fluids Engineering*, vol. 103, no. 3, pp. 456–460, Sep. 1981, doi: 10.1115/1.3240815.